Piezoelectric nanoelectromechanical systems integrating microcontact printed lead zirconate titanate films

Daisuke Saya, Denis Dezest, Aaron Welsh, Fabrice Mathieu, Olivier Thomas, Thierry Leichle, Susan Trolier-Mckinstry, Liviu Nicu

▶ To cite this version:

Daisuke Saya, Denis Dezest, Aaron Welsh, Fabrice Mathieu, Olivier Thomas, et al.. Piezoelectric nanoelectromechanical systems integrating microcontact printed lead zirconate titanate films. Journal of Micromechanics and Microengineering, 2020, 30 (3), pp.035004. 10.1088/1361-6439/ab60bf . hal-02453806v2

HAL Id: hal-02453806

https://hal.science/hal-02453806v2

Submitted on 16 Nov 2020

HAL is a multi-disciplinary open access archive for the deposit and dissemination of scientific research documents, whether they are published or not. The documents may come from teaching and research institutions in France or abroad, or from public or private research centers.

L'archive ouverte pluridisciplinaire **HAL**, est destinée au dépôt et à la diffusion de documents scientifiques de niveau recherche, publiés ou non, émanant des établissements d'enseignement et de recherche français ou étrangers, des laboratoires publics ou privés.

Piezoelectric nanoelectromechanical systems integrating microcontact printed PZT films

Daisuke Saya[1], Denis Dezest[1], Aaron J. Welsh[2], Fabrice Mathieu[1], Olivier Thomas[3], Thierry Leïchlé[1], Susan Trolier-McKinstry[2] and Liviu Nicu[1]

[1]LAAS-CNRS, University of Toulouse, 7 Avenue du Colonel Roche, 31077 Toulouse, France

[2]Department of Materials Science and Engineering and Materials Research Institute, The Pennsylvania State University , N-227 Millennium Science Complex, University Park, PA 16802 USA

[3]Laboratoire des Sciences de l'Information et des Systèmes, 8 boulevard Louis XIV 59000 Lille, France

E-mail: dsaya@laas.fr

ABSTRACT

A piezoelectric nanoelectromechanical system (NEMS) with integrated actuation and detection capabilities was fabricated using lead zirconate titanate (PZT) thin films patterned by microcontact printing. PZT-coated cantilever resonators of various dimensions were fabricated to assess the variability in PZT properties as a function of the device dimensions; the microcontact-printed PZT was 281 nm thick. PZT layers of the cantilevers were poled at 107 kV/cm and 150 °C to improve their piezoelectric properties. It was demonstrated that PZT piezoelectrics can be utilized for simultaneous actuation and detection of resonance. The PZT cantilevers were analytically modelled to estimate values of their piezoelectric coefficient d_{31}. Mechanical tip displacement detection of the cantilevers by laser vibrometer was also carried out to validate the estimation of d_{31}.

I. INTRODUCTION

Over the last decade, advances in nanofabrication technology and electromechanical systems have led to the emergence of nanoelectromechanical systems (NEMS). NEMS-based resonators have significantly enhanced device performance through size reduction.[1-12] Specifically, mechanical resonators with free-standing structures of nanometer scale cantilevers or bridges have high sensitivities for mass sensing applied to gas[4,5] and biomolecule[6,7] detection. NEMS structures are fabricated two ways; bottom-up fabrication produces nanoresonators with potentially smaller sizes and thus higher sensitivities in mass detection,[4,5] top-down fabrication techniques enable mass production and integration with electrical circuits.[6-12]

Piezoelectric films, which translate mechanical energy into electrical and vice-versa, have widely been used for microelectromechanical systems (MEMS) transduction, i.e. actuation and detection.[9-21] Of the various transduction mechanisms used in MEMS devices, piezoelectricity requires relatively low actuation voltage and offers the possibility of sensing, resulting in integrated devices that are compact, and thus potentially portable.[13-16,20,21] In this regard, piezoelectric films could be particularly advantageous for transduction in NEMS, since there are few solutions suited to both actuation and sensing at this scale. However, studies have shown that some sputtered PZT films on NEMS resonators displayed reduced performance,[17,18] likely as a result of a deterioration of the films' piezoelectric characteristics with reduced thickness. Recently, microcontact printed PZT films were found to retain their characteristics with reduced lateral dimensions and thicknesses.[19,20]

The aim of this work is thus to prove that microcontact printed PZT films are good candidates for efficient NEMS transduction. For this, silicon cantilevers of various dimensions integrating microcontact printed

PZT thin film were fabricated and characterized. The PZT cantilevers were assessed for piezoelectric excitation and detection. The effect of poling on the piezoelectric characteristics of the PZT was investigated. Then, the PZT cantilevers were analytically modeled as laminated beams for estimations of their piezoelectric coefficient d_{31}, with a measure of the electrical charge created in the piezoelectric layer for a given excitation voltage around a given resonance. This method was also validated by resonance measurements by means of a laser vibrometer.

II. FABRICATION OF SILICON CANTILEVERS WITH MICROCONTACT PRINTED PZT FILM

Fabrication of PZT-coated cantilevers was carried out using SOI (silicon on insulator) wafers with a 340 nm top Si layer, 1 μm thick buried SiO_2 and a 525 μm thick bulk Si handle wafer. An ultraviolet (UV) stepper photo repeater (I-line FPA 3000 Canon Inc.) was used for all lithography steps since high resolution and precise alignments were desirable for top-down NEMS fabrication.

First, a 100 nm thick SiO_2 film was grown by thermal oxidation and a 60 nm thick hafnium dioxide (HfO_2) film was deposited by atomic layer deposition (ALD) to create a barrier against Pb diffusion (Fig. 1.1). The deposition occurred at 200 ˚C with a chamber pressure of 0.72 Torr. The reactant pulse time for H_2O and tetrakis(ethylmethylamino)hafnium (TEMAH) was 0.03 and 0.15 s respectively, with a purge time of 10 s between each pulse. These cycles were repeated 619 times to create an amorphous 60 nm thick HfO_2 layer which was crystallized with a 700 ˚C heat treatment in an O_2 ambient for 1 min. A 30 nm titanium adhesion layer was sputtered at room temperature using a power of 200 W, a bias of 460 V, a current of 0.47 A, a deposition pressure of 2 mTorr, and an Ar flow rate of 8 sccm, for 300 s. Without breaking vacuum, a 125 nm Pt bottom electrode was sputtered at room temperature using a power of 200 W, a bias of 580 V, a current of 0.34 A, a deposition pressure of 2.5 mTorr, and an Ar flow rate of 11 sccm, for 417 s (Fig. 1.2). Next, the cantilever was defined by reactive ion etching (RIE). For this purpose, after patterning a photoresist layer with the stepper, a 540 nm nickel layer to be used as the hard mask during ion etching was deposited by electroplating. Successive reactive ion etching of Pt, Ti, HfO_2, SiO_2 and top Si layer was performed until reaching the buried SiO_2 layer (Fig. 1.3). Then, the nickel hard mask was removed using the nickel etchant TFB (Nitric acid aqueous solution). Microcontact printing of the PZT film was then performed on top of the electrode patterned on the silicon structure (Fig. 1.4). For printing, a PZT sol-gel solution (1 % Mn doped, with atomic percentage Pb=110 %, Zr=30 %, Ti=70 %, Mn=1 %), from Mitsubishi Materials were spin-coated onto a polydimethylsiloxane (PDMS) stamp with a polyurethane layer that improved wetting of the PZT solution[19]. The PZT sol-gel solution was transferred onto the entire surface of the chip by manually pressing the stamp, and the film was pyrolyzed at 350 °C for 300 s and subsequently crystallized at 650 °C for 60 s. This printing process was repeated seven times to achieve a final film thickness of 281 nm (Fig. 1.4). The resulting films showed microstructures characteristic of the perovskite phase, with a small amount of pyrochlore observed at triple points. Printed 30/70 PZT features exhibited a relative permittivity of 500 and a loss tangent of 0.9 %. The hysteresis loops were well formed, without pinching of the loops. The patterned features showed remanent polarizations of 27 $\mu C/cm^2$, and coercive fields of 110 kV/cm. Since the cantilever and bottom electrode was defined before the PZT printing step, as shown in Fig. 1.3, there was no need for precise alignment during stamping to achieve PZT film patterning on the cantilever.

In order to access the bottom electrode, the PZT film was patterned by wet etching in buffered hydrofluoric acid (BOE) after a photolithography step using SPR1813 photoresist (Fig. 1.5). Then, the Ti/Pt bottom

electrode was patterned by reactive ion etching with a 6 μm thick photoresist mask (Fig. 1.6) and a 30 nm thick Pt top electrode was patterned by lift off (Fig. 1.7). For this step, ZEP520A electron beam resist was patterned via electron beam lithography (EBPG 5200, Vistec) using a beam current of 40 nA, a dose of 365 $\mu C/cm^2$, an aperture size of 400 μm, and a beam step size of 25 nm. After development of the photoresist, the Pt was sputtered and lifted off.

The next step was dedicated to patterning the ground plane, in order to allow the top Si layer of the SOI wafer to be electrically grounded (not shown in Fig. 1). This process consisted first of etching the HfO_2 and SiO_2 films to expose the top Si layer everywhere on the chip surface, except at the electrode and cantilever locations. Then Ti/Al (100 nm/ 700 nm) was deposited on the exposed Si surface. This metallization of Ti/Al was done at the same time as the metallization of the electrical circuits in the following step (Fig. 1.9). As discussed in section III. A, this step eliminated the parasitic capacitance between the electrodes and the device Si layer.

In order to prevent electrical shorts between the bottom electrode and the Ti/Al electrode deposited in the following process, a 100 nm thick Si_3N_4 insulating film was patterned by lift-off using a bi-layer 300 nm thick LOR3A and 1 μm thick ECI photoresist (Fig. 1.8). The LOR3A layer was used to facilitate the lift-off process due to the re-entrant profile. The Si_3N_4 insulating film was deposited by inductively-coupled plasma chemical vapor deposition (ICPECVD) in order to ensure a uniform and conformal deposition over the step formed by the bottom electrode and PZT layer. Electrical connections were made by lift-off patterning of 100 nm/ 700 nm Ti/Al using 2.6 μm thick nLOF photoresist (Fig. 1.9). Finally, backside etching for cantilever release was performed by deep reactive ion etching of the handle Si wafer using a 40 μm thick AZ40XT photoresist mask, followed by etching of the buried SiO_2 layer (Fig. 1.10). Scanning electron microscopy photographs of the fabricated PZT covered cantilevers are shown in Fig. 2.

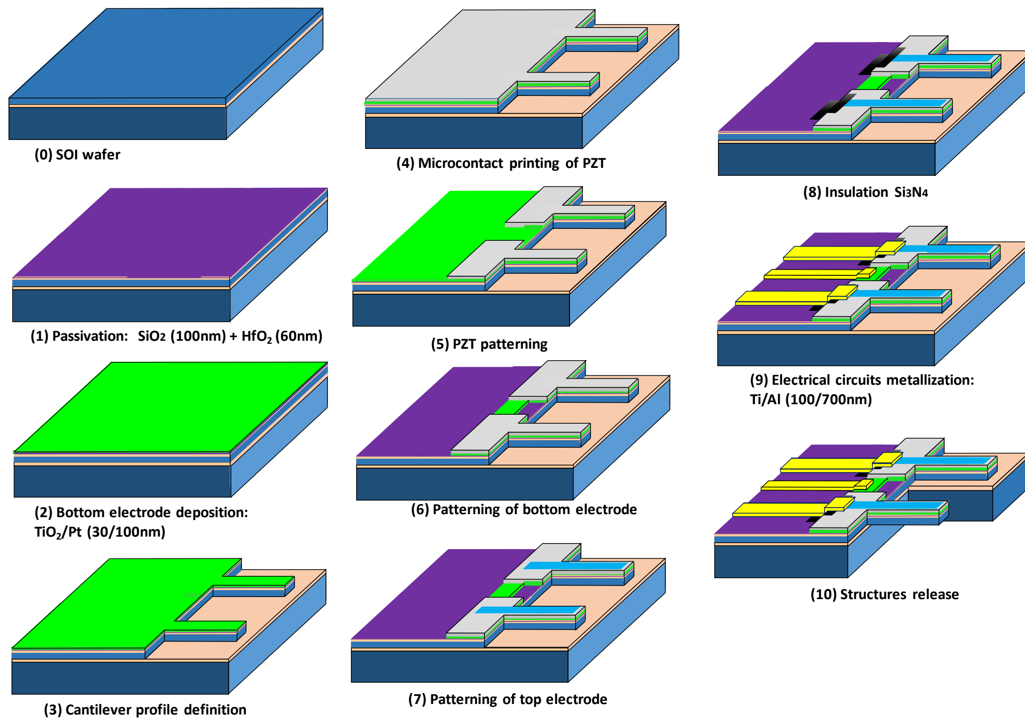

FIG. 1. Fabrication process of free-standing silicon cantilevers with microcontact printed PZT films.

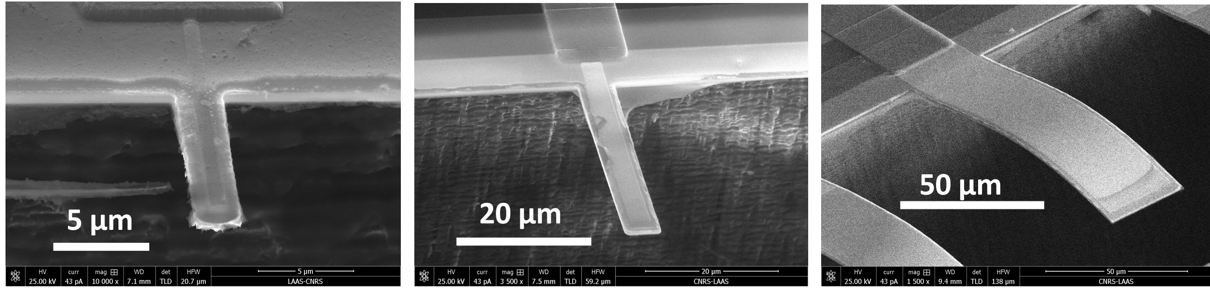

(a) (b) (c)

FIG. 2. SEM images of cantilevers with microcontact printed PZT films. (a) Short (10 µm long), (b) medium size (35 µm long) and (c) long (150 µm long) PZT coated cantilevers.

Each cantilever is a multilayer composed of 300 nm thick Si, 100 nm thick SiO_2, 60 nm thick HfO_2, 30 nm/100 nm thick Ti/Pt layers as the bottom electrode, 281 nm thick microcontact printed PZT layer, and 30 nm thick Pt top electrode, as shown in Fig. 3. An unreleased cantilever with exactly the same structure was integrated onto the same chip, serving as a reference to compensate the static capacitance of the piezoelectric stack during electrical characterization, as described in section III. A.

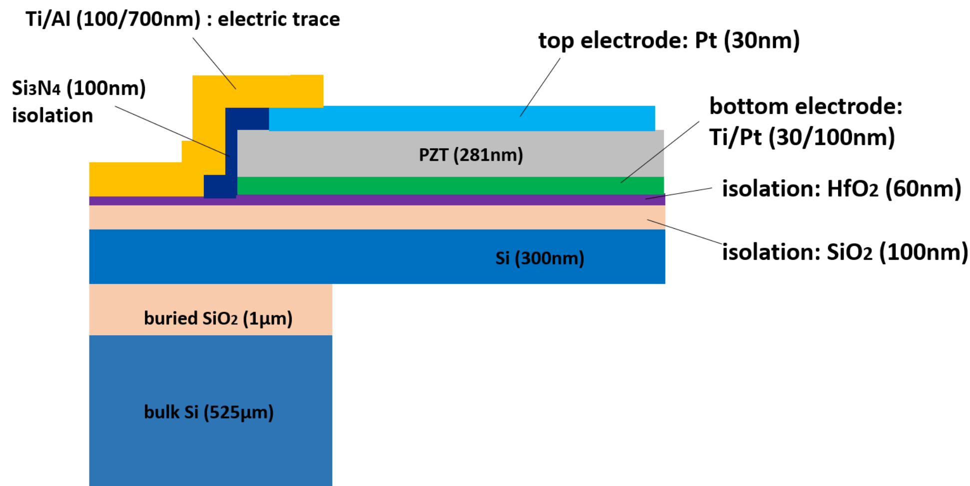

FIG. 3. Scheme of the integrated piezoelectric stack.

Three different types of cantilevers (depicted in Table I) were designed in order to study possible dimensional effects upon PZT film properties: the short cantilevers are 10 µm long and 2 µm wide. The medium size cantilevers are 35 µm long, 5 µm wide. Lastly, the long cantilevers are 150 µm in length and 30 µm in width.

TABLE I. Dimensions of the fabricated cantilevers.

	Short cantilever	Medium cantilever	Long cantilever
Length	10 µm	35 µm	150 µm
Width (except top Pt layer)	2 µm	5 µm	30 µm
Width (top Pt layer)	1 µm	3 µm	26 µm

III. MEASUREMENT OF THE CANTILEVER RESONANCE FREQUENCY USING THE PZT PIEZOELECTRIC RESPONSE

A. Electrical set-up

A schematic of the apparatus used for resonance frequency measurements[16,20] is shown in Fig. 4. To operate the device, a sinusoidal voltage V_1 was applied between the top and bottom electrodes on the piezoelectric layer, leading to the motion of free-standing cantilevers due to the converse piezoelectric effect. An opposite voltage $-V_2$ was also applied to an unreleased structure with the same dimensions which served as a reference to reduce the effect of the static capacitance of the PZT layer. The charges generated by the two structures were collected by the common bottom electrode and were amplified through a charge amplifier (1 V/pC gain). The signal was then injected into a demodulator to extract both amplitude and phase.

The top Si layer was grounded to eliminate the charges generated by the parasitic capacitances C_1 and C_2, and the charges from C_s were compensated by the reference; where C_1 is the parasitic capacitance between the top electrode trace line and the top Si layer of the SOI, C_2 is the parasitic capacitance between the bottom electrode line and the top Si layer of the SOI, C_s is the static capacitance of the PZT (dielectric) layer sandwiched between the top and bottom electrodes, and C_{mot} is the motional capacitance corresponding to the charges generated by the PZT layer during the resonator motion due to the direct piezoelectric effect.

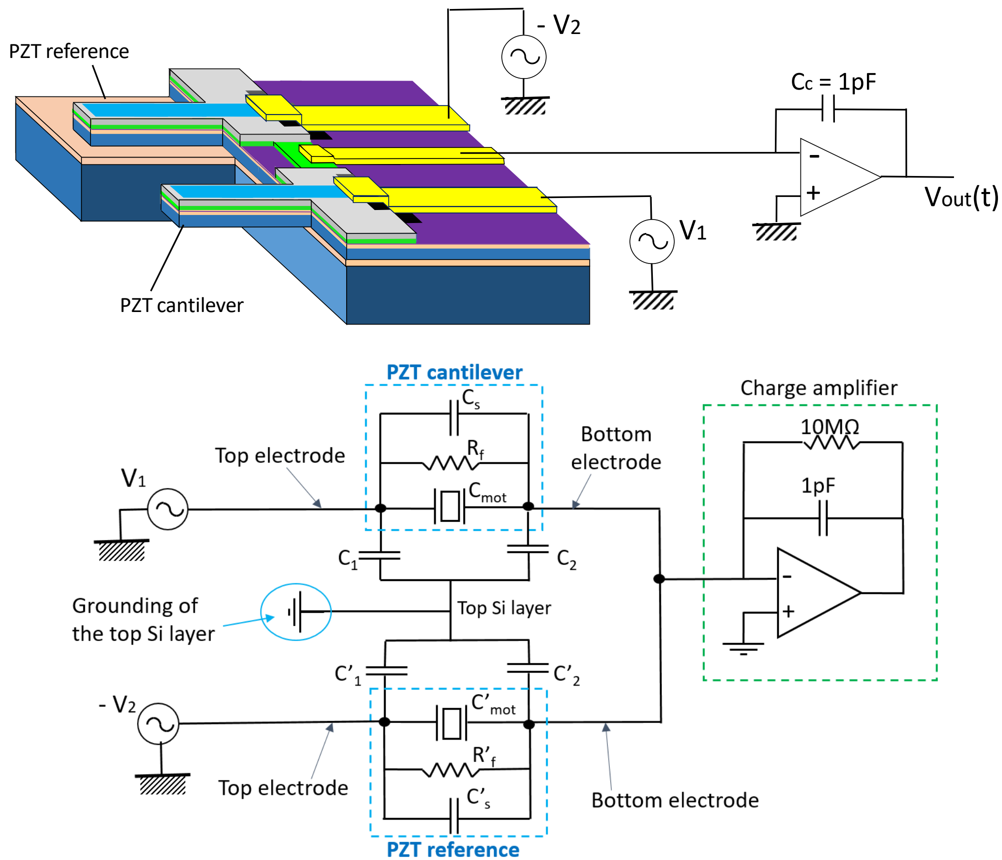

FIG. 4. Schematic sketch of electrical detection. Electrical connections of the device (up), details of the measurement electronics including the electrical model of the cantilevers (bottom).

B. Detection of resonance frequency by piezoelectric response and effect of poling on PZT films

Using this electrical set up, the resonance frequencies of the medium size and long PZT cantilevers were detected through their piezoelectric responses. At first, the measurements were done without poling treatment of the PZT films. In order to improve the PZT layer properties and obtain a larger amount of charges upon cantilever deflection, the PZT was poled[20,22-29] by applying 3 V between the top and bottom electrodes (i.e. 107 kV/cm across the 281 nm thick PZT layer) at a temperature of 150 °C. A commercial Cascade Summit 12000 probe station allowed the Si chips to be heated while placing needle probes on the electrodes in order to pole the PZT and a Keithley 4200 was used to apply the DC voltage between the top and bottom electrodes.

The frequency spectra of the first mode resulting from the charges generated by the PZT layer with variation of poling time are shown in Fig. 5. In the case of the long cantilevers (Fig. 5(a)), even before poling, the resonance frequency could be detected using an actuation voltage (V_1) of 100 mV as shown in Fig. 5(a) "Before poling". After 15 minutes of poling, the amplitude of the resonance peak increased by 33 %. By poling for 120 min more (for a total of 135 min), the charges generated at the resonance peak increased further to 230 fC (from an unpoled value of 120 fC). The detected resonance frequency of the first mode was 18.3 kHz and quality factor in air was 67. The second and third modes were also detected: 102.3 kHz with a Q factor of 182 and 291.6 kHz with a Q factor of 266, respectively.

In the case of the medium size cantilevers (Fig. 5(b)), the effect of poling was more remarkable. Before poling, the charge detected at resonance was only 1.4 fC for an actuation voltage of 700 mV. However, after 15 minutes of poling, the charges generated at resonance were found to dramatically increase up to 10 fC for an actuation voltage of 100 mV. By applying the poling protocol for 120 min more (for a total of 135 min), the generated charges further increased to 29.6 fC. The detected resonance frequency of the first mode was 473 kHz and the quality factor in air was 223. The second mode was 2.36 MHz with Q factor 388. For both long and medium size cantilevers, extending the poling treatment to a total of 255 min (120 min more) did not lead to any observable enhancement of the generated charges level (data not shown). Thus, 135 min of poling time maximized the PZT properties.

As for the short cantilever (10μm in length, 2μm in width), Figure 5(c) shows that before poling, the resonance frequency could not be detected. However, after performing a 135 min poling step, the resonance frequency was detectable. The amount of charges generated at resonance was 0.56 fC for an actuation voltage of 20 mV. The measured resonance frequency was 5.72 MHz with a quality factor in air of 381. Hence, the capability of simultaneous actuation and detection of the cantilevers using microcontact printed PZT layers was validated even with the short cantilever.

For the medium and short cantilevers, the measured first mode resonance frequencies of 473 kHz and 5.72 MHz, respectively, are about 8 % smaller than the simulated value of 508.0 kHz and 6.215 MHz, obtained with the analytical model of a laminated beam described in section IV. A.[30,31] As will be discussed in sections IV. A and IV. E, these slight differences may be attributed to non-ideal clamping of the cantilevers.

In the case of the long cantilever, the measured fundamental mode was 18.2 kHz while the simulated one was 27.75 kHz. Hence, the difference between experimental and theoretical resonance frequency values reaches 52 % in the case of long cantilevers. This large discrepancy is believed to be a consequence of a decrease in the cantilever's thickness due to overetching during fabrication. According to the analytical model which will be mentioned in section IV. A, the Si layer thickness of the long cantilever may be

decreased to 90 nm. It is because of non-uniformity in etching speed of the deep reactive ion etching of the handle Si wafer during the release of the cantilever structures (Fig. 1.10). The etching speed is slower on the edge of the etching patterns. The medium and the short cantilevers are situated on the edge of the etching patterns. Hence, while the etching for releasing long cantilever is about to be finished, the medium and the short cantilevers are not yet released. To complete the release process of all cantilevers, the long cantilevers may suffer from this overetching.

As can be seen in Fig. 5, the measured resonance frequencies slightly increase after the 135 min poling treatment, for the long cantilever from 18.2 kHz (before poling) to 18.3 kHz (after 135 min poling) and for the medium cantilever from 466.6 kHz (before poling) to 473.2 kHz (after 135 min poling). This results can be attributed to the remanent strain induced by the alignment of the PZT dipoles towards the direction of the applied field during poling;[24,25] the resulting in-plane contraction[26,27] should have produced a curvature change of the cantilevers. For these poling conditions, aging[28,29] was limited, as demonstrated by the stability of the resonance peak amplitudes during measurements spanning a period of two months.

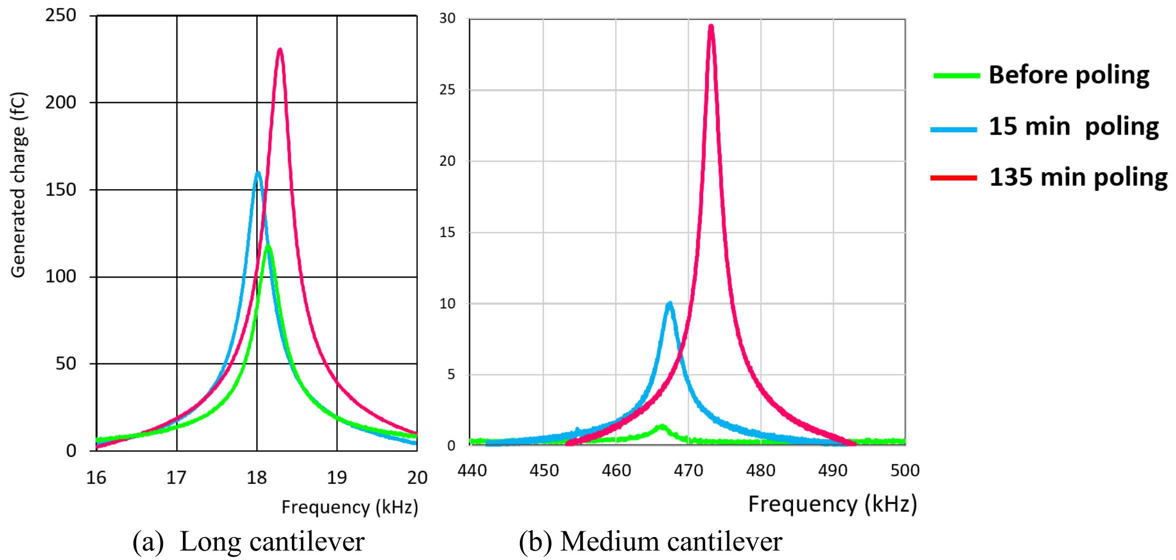

(a) Long cantilever (b) Medium cantilever

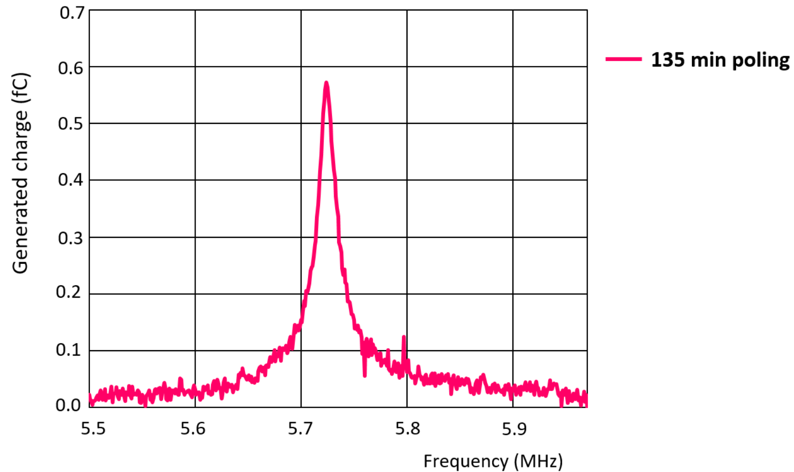

(c) Short cantilever

FIG. 5. Resonance spectra with variation of poling time. (a) 150 μm long cantilever actuated with V_1 = 100 mV, (b) 35 μm long (medium size) cantilever actuated with V_1 = 700 mV before poling and 100 mV after poling, and (c) 10 μm long (short size) cantilever actuated with V_1 = 20 mV after poling.

IV. ESTIMATION OF THE PIEZOELECTRIC COEFFICIENT d_{31}

Estimation of the piezoelectric coefficient d_{31} was done by modeling the PZT cantilever as a laminated beam and by comparing the result of the model to two sets of experimental results at a particular resonance. First, the motional capacitance C_{mot} was obtained from impedance data at resonance, from which the piezoelectric response was extracted. Secondly, the displacement of the tip of the cantilever as a function of the voltage applied to the piezoelectric layer was detected by a laser vibrometer. This was modeled using equivalent single layer beam theory for the laminated beam, with all details given in the Appendix. The following section presents a comparison of the analytical model and finite element model (FEM, ABAQUS) used for model validation and then the method used to determine the d_{31} coefficient.

A. Validation of the beam model with finite element computations – modal analysis

As explained in the Appendix, the kth natural frequency is given by the equivalent single layer beam model of the cantilever:[30]

$$f_k = \frac{\beta_k^2}{2\pi L}\sqrt{\frac{\hat{D}}{m}} \tag{1}$$

with $\beta_1 = 1.875$, $\beta_2 = 4.694$, etc. and where $\hat{D}$ is the bending stiffness and m is the mass per unit length of the beam. These results were compared with a three-dimensional finite element model of the structures, built in the commercial code ABAQUS. The three cantilevers defined in Tables I and II were considered.[32,33] The finite-element meshes are shown in Fig. 6. Each physical layer of the cantilevers is meshed with one layer of hexahedral finite elements with 20 nodes and quadratic shape functions (C3D20 finite elements), that include electric degrees of freedom for the PZT layer (C3D20E finite elements). The convergence was checked with refined meshes; those results are less than 0.1 % different than the meshes of Fig. 6. Figure 7 shows the mode shapes of some bending modes of the cantilevers obtained by finite element simulations with ABAQUS.

TABLE II. Properties of layers of the cantilever.[32,33]

	Thickness (nm)	Mass density (kg/m^3)	Young's modulus (GPa)
Pt (top)	30	21450	145
PZT	281	7800	105
Pt (bottom)	100	21450	145
Ti	30	4510	110
HfO_2	60	9700	57
SiO_2	100	2150	70
Si	300	2500	169

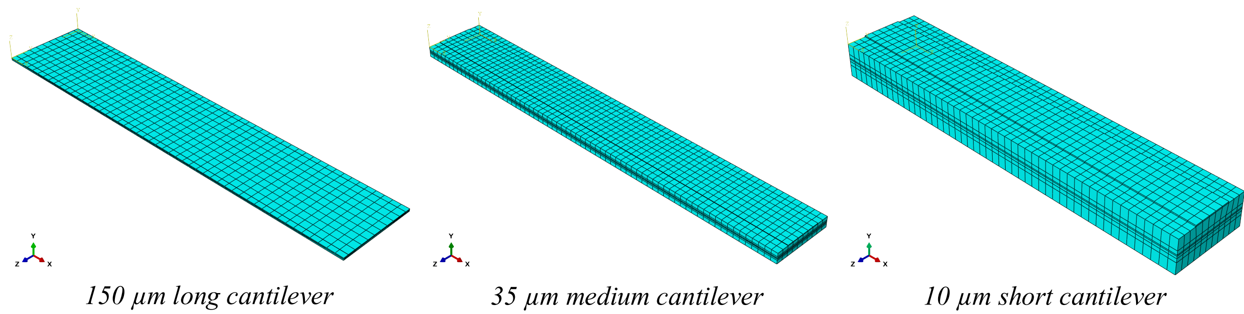

FIG. 6. Meshes used in the FE computations.

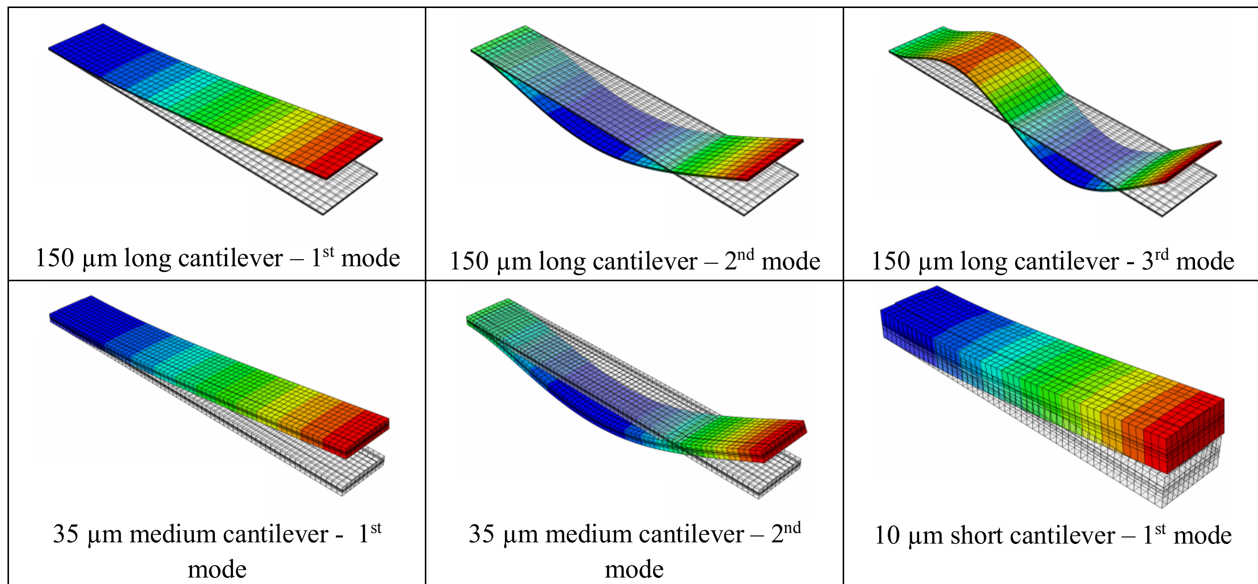

FIG. 7. Mode shapes of some bending modes of the cantilevers obtained by finite element simulations with ABAQUS.

Figure 8 and Table III show the natural frequencies of the beam obtained by the single layer model as a function of the ones obtained by the finite element computations. A difference of about 3 % is observed between the two approaches. Considering the aspect ratios of the cantilevers (close to a thin plate for the 150 µm long cantilevers and close to a thick beam with a small aspect ratio for the 10 µm short cantilevers), as well as their complex lamination (7 layers), this error can be considered very small, which validates the equivalent single layer beam model. We also compared the natural frequencies of the cantilevers for different electrical boundary conditions (without piezoelectric effects, PZT layer in short circuit and PZT layer in open circuit) with d_{31}=10 pm/V for the piezoelectric coefficient. Differences less than 0.1 % where noticed, which is consistent with the small piezoelectric coupling factor (less than 1 %) associated to this d_{31} value (see a reference[34] for details about the piezoelectric effect on the natural frequencies in short and open circuit and their relation to the electromechanical coupling factor).

The experimental frequencies of the cantilevers of section III. B are also shown in Fig. 8. A line of slope 1 is provided, showing good agreement between the experimental and theoretical values of the resonance frequencies. It is notable that the experimental natural frequencies are smaller than those predicted by the theory. This can probably be explained by the non-ideal clamping with a smaller stiffness in experiments

than in theory, as will be shown in Fig. 14, as well as some unavoidable uncertainties on the material constants values of the six materials used in the complex lamination of the beams. In the case of the long cantilever, the reduction in experimental natural frequency was caused by overetching during fabrication, as discussed in section III. B.

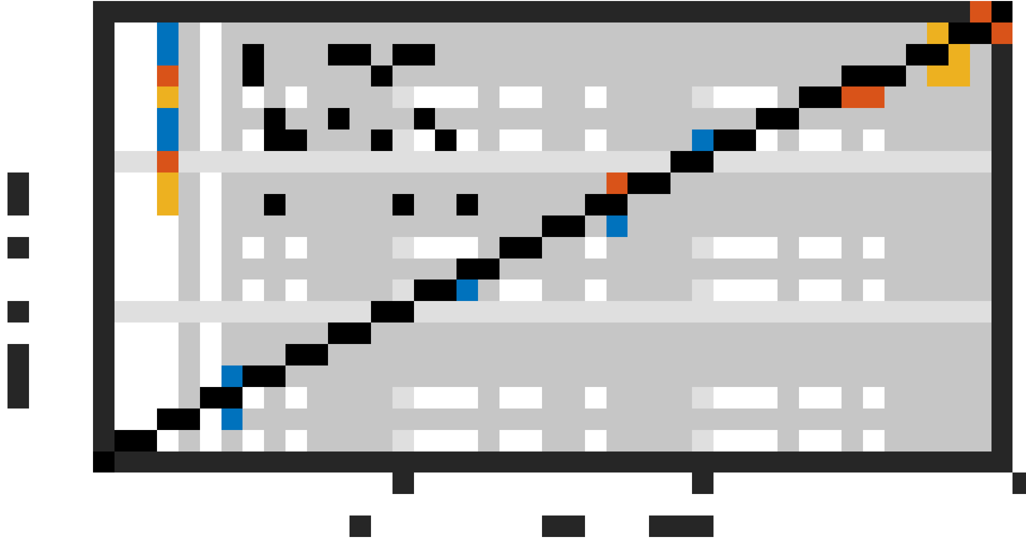

FIG. 8. Experimental (Exp.) resonance frequencies and finite element (ABAQUS) natural frequencies as a function of theoretical (equivalent single layer beam theory) natural frequencies of the cantilevers. The dashed line has a slope of one.

TABLE III. Comparison of natural frequencies from the equivalent single layer beam theory and the reference 3D finite element computation.

	150 μm long cantilever			35μm medium cantilever		10μm short cantilever
	Mode 1	Mode 2	Mode 3	Mode 1	Mode 2	Mode 1
Single layer beam theory [kHz]	27.75	173.95	487.06	508.03	3184.1	6214.5
Finite elements [kHz]	27.09	169.54	475.44	492.63	3074.8	5985.90
Error [%]	2.39	2.53	2.39	3.0	3.4	3.68

B. Validation of the beam model with finite element computations – frequency response functions with piezoelectric effect.

The mechanical frequency response (FRF) of the cantilevers determined by the equivalent single layer theory and by realistic finite-element computations was compared. A sinusoidal voltage of frequency Ω was applied to the PZT layer $V(t) = V_0 cos\Omega t$. The resulting tip displacement $w_t(t) = w_{t0} cos(\Omega t + \varphi)$ of the cantilevers by both models was then calculated and compared. The amplitude of the frequency response is simply $H(\Omega) = w_t/V_0$. For the finite-element computations, the frequency response is obtained at each frequency Ω with an inversion of the dynamical stiffness matrix (direct steady-state dynamics in ABAQUS). A mass-proportional damping is used, for which the damping matrix is $C = aM$, where M is the mass matrix.

a was chosen so that quality factors between 10 to 200 were obtained for the modes of interest for the three cantilevers (short cantilever: $a = 10^6\ \mathrm{s}^{-1}$, medium cantilever: $a = 50.10^3\ \mathrm{s}^{-1}$, long cantilever: $a = 20.10^3\ \mathrm{s}^{-1}$). For the kth angular natural frequency, ω_k, computed by the finite element model, $Q_k = \omega_k/\alpha$. For the analytical model, Eq. (A.11) and (A.14) in the Appendix are used. All the other parameters (χ_k, m, L) were computed with the geometrical and material characteristics of the cantilevers (Tables I and II). Moreover, the width b_p of the piezoelectric layer used in Eq. (A.4) in the Appendix to compute the piezoelectric constants Θ and Ξ was set equal to the top electrode width (see Table I), since most of the electric field lines created in the PZT layer encompass the volume just below the top electrode. Besides, in the analytical model, the electric field in the piezoelectric layer is independent of y.

Figure 9 shows $H(\Omega)$ for the three cantilevers, computed by the single layer theory and the finite-element model. Very good agreement is obtained for the three cantilevers, with a slight underestimation of the frequency response by the analytical model. This effect is mainly observed in the case of the first mode of the short cantilever. This can be explained by the relatively large aspect ratio of this cantilever (the ratio between its length and the cross-sectional thickness is 11 for the short cantilever, see Fig. 10), for which the Euler-Bernoulli theory is at its limits. Moreover, as shown in Fig. 10, there are fringing electric field lines in the PZT layer that extend beyond the top electrode, which results in an increased active PZT volume with respect to that considered in the analytical model. Those effects are smaller for the medium and the long cantilever, with larger aspect ratios (38 and 166, respectively). Given the good agreement between measured and modeled response, the analytical model can be used for the d_{31} piezoelectric coefficient estimations.

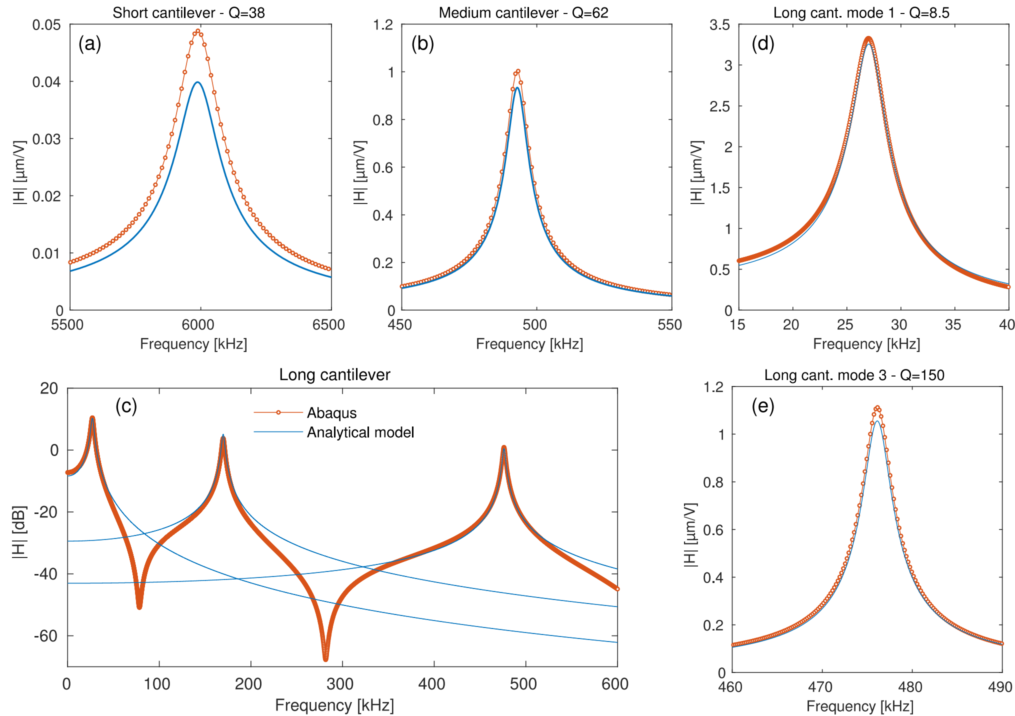

FIG. 9. Frequency response functions: tip displacement of the cantilevers for a unit voltage in the PZT layer as a function of driving frequency. Comparison between reference finite element computation results with ABAQUS (orange lines) and results from the equivalent single layer model (blue lines. Solid: 4 mode model; dashed: single mode model).

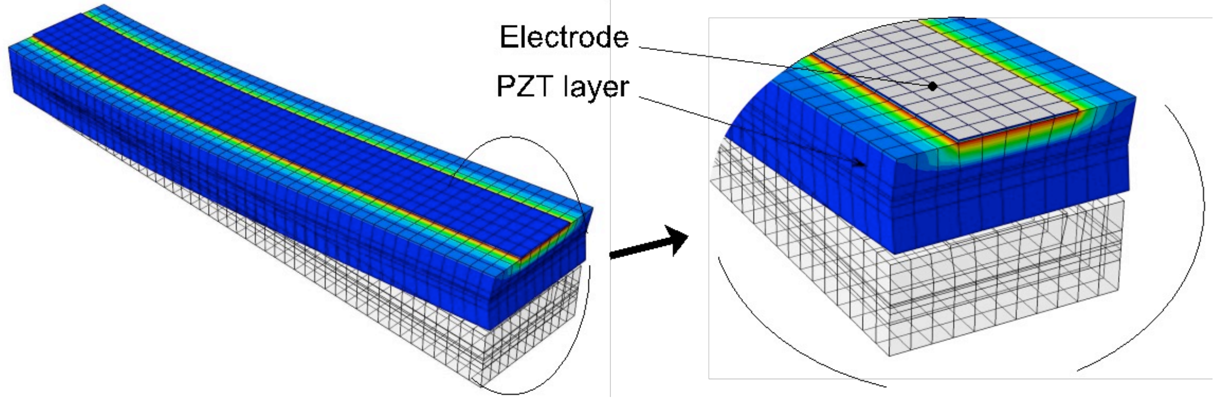

FIG. 10. Deformed shape at the first resonance of the short cantilever with the electrical potential shown in color.

C. Estimation of the d_{31} coefficient

The d_{31} piezoelectric coefficient was estimated by measuring the motional capacitance C_{mot} of the cantilevers (the ratio between the number of piezoelectrically created electric charges and the input voltage) at a specific resonance. The piezoelectric response in the analytical model was then adjusted so that the modeled response fit the experimental data. This method has been used successfully in a previous work.[18] As shown in the Appendix (Eq. (A.19), the motional capacitance C_{mot} for the cantilevers can be written as:

$$C_{\mathrm{mot}} = \alpha\, d_{31}^2 \quad \text{with} \quad \alpha = \frac{Q_k Y_p^2 \hat{\hat{\Theta}}^2 \Phi_k'^2(1)}{m L^3 \omega_k^2} \tag{2}$$

The α parameter ([N/m]) is a function of the kth eigenmode (quality factor Q_k, natural frequency ω_k and mode shape slope at the tip Φ_k'), the Young's modulus of the PZT layer Y_p, the length L of the cantilever and the piezoelectric constant $\hat{\hat{\Theta}}$ proportional to the PZT layer mean height with respect to the neutral line of the cantilever.

For each cantilever, d_{31} is estimated by:

$$d_{31=} \sqrt{\frac{C_{\mathrm{mot}}}{\alpha}} \tag{3}$$

where C_{mot} is obtained by recording the resonance spectra as a function of actuation voltage and α is computed using the values of Tables I and II for Y_p, L and $\hat{\hat{\Theta}}$, the theoretical mode shapes for Φ_k' (Eq. (A.10) in the Appendix) and the experimental values of Q_k and ω_k.

Figure 11(a) shows the 1st mode resonance response of the motional capacitance (for cantilevers after 135 min poling treatment). A plot of the generated charges as a function of actuation voltages at resonance shows excellent linear behavior (Fig. 11(b)), permitting determination of the experimental values of C_{mot}. In the case of the long PZT cantilever, the applied voltage V_0 varied from 25 mV to 125 mV (Fig. 11(1)) and in the case of the medium PZT cantilever, it varied from 50 mV to 300 mV (Fig. 11(2)). The average quality factor and experimental values of C_{mot} were estimated to be 67 and 223, and 2.306 fC/mV and 0.296 fC/mV, respectively for the long and medium cantilever. For the short PZT cantilevers, with applied voltage V_0

ranging from 10 mV to 100 mV (Fig. 11(3)), the average quality factor and the experimental values of C_{mot} were estimated to be 381 and 0.026 fC/mV.

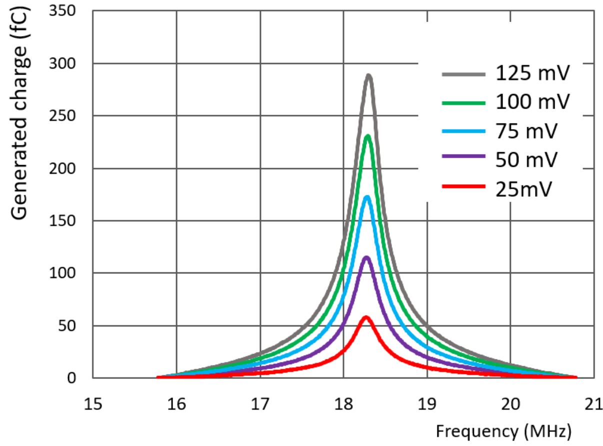

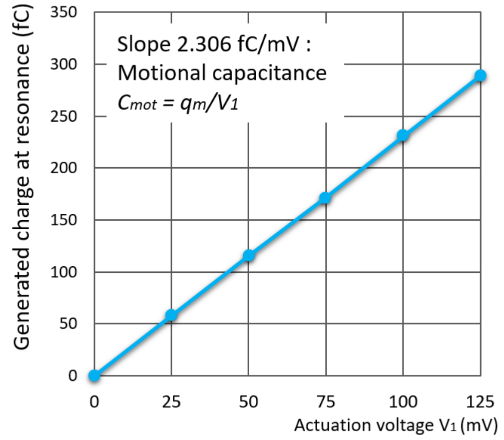

(a) (b)

(1) Long PZT cantilever: 150 μm in length, 30 μm in width

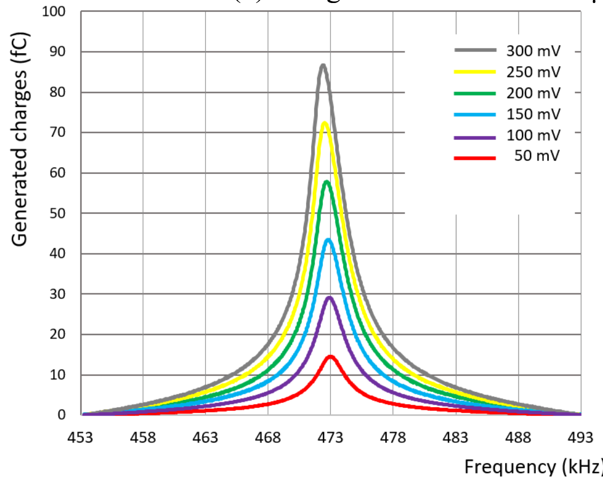

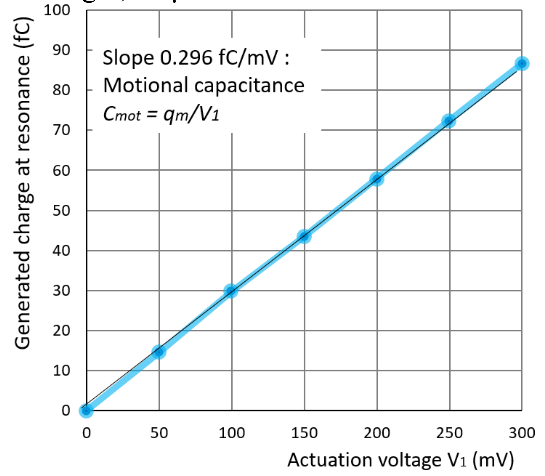

(a) (b)

(2) Medium PZT cantilever: 35 μm in length, 5 μm in width

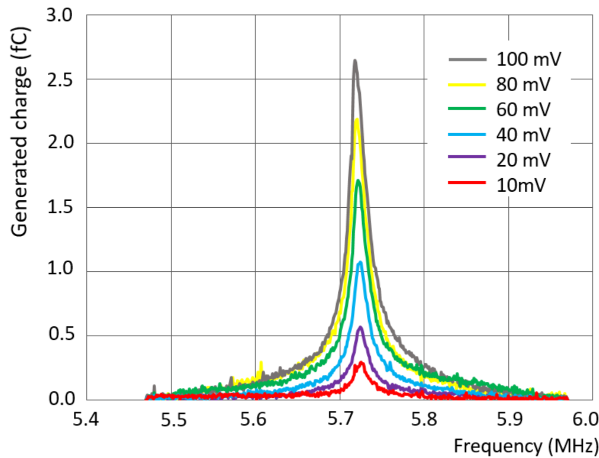

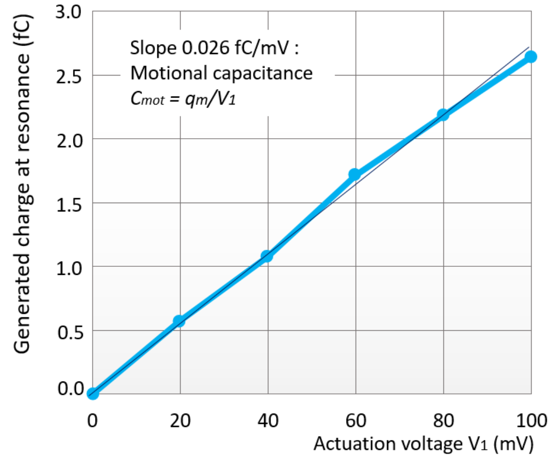

(a) (b)

(3) Short PZT cantilever: 10 μm in length, 2 μm in width

FIG. 11. (a) Piezoelectric responses of the PZT cantilevers as a function of actuation voltage after a 135 min poling process, (b) slope of the generated charge at the resonance peak as a function of actuation voltage.

D. Estimated values of the d_{31} coefficient and its evolutions with poling time

The piezoelectric coefficient d_{31} was calculated using the motional capacitance C_{mot} and quality factors estimated in the previous section. Piezoelectric coefficients d_{31} of -6.9 ± 0.1 pm/V, -12.0 ± 2.0 pm/V and -11.0 ± 2.4 pm/V were calculated respectively for the long, medium size and short cantilevers for the first mode. These calculated values of d_{31} were smaller than those previously reported,[19,21] where values of d_{31} were estimated to be around 50 pm/V for PZT films with a thickness in the 100 -200nm range. These lower values are due to the use of a PZT composition off of the morphotropic phase boundary, as well as potential degradation of PZT layer induced by the presence of hydrogen[35] most probably during ICPECVD process for deposition of Si_3N_4 film (Fig. 1.8), even though annealing of 400 °C 30 min in N_2 atmosphere was conducted to eliminate hydrogen molecules from the PZT layer.

The d_{31} values were calculated for each poling time for serval cantilevers of each size. The evolution of d_{31} values as a function of poling time are shown in Fig. 12 and Table IV. In the case of the medium size cantilever, the generated charges at resonance before poling treatment were very low (1.4 fC with 700 mV actuation voltage), leading to 1.2 pm/V for the d_{31} coefficient which is not unexpected for an unpoled piezoelectric. However, after 135 minutes of poling, the d_{31} value became comparable to that of the PZT film integrated into the long cantilever. As for the short cantilever, the d_{31} value was also comparable to that of the long cantilever PZT film after the poling process. The d_{31} values did not show any significant increase when the poling time exceeded 135 min.

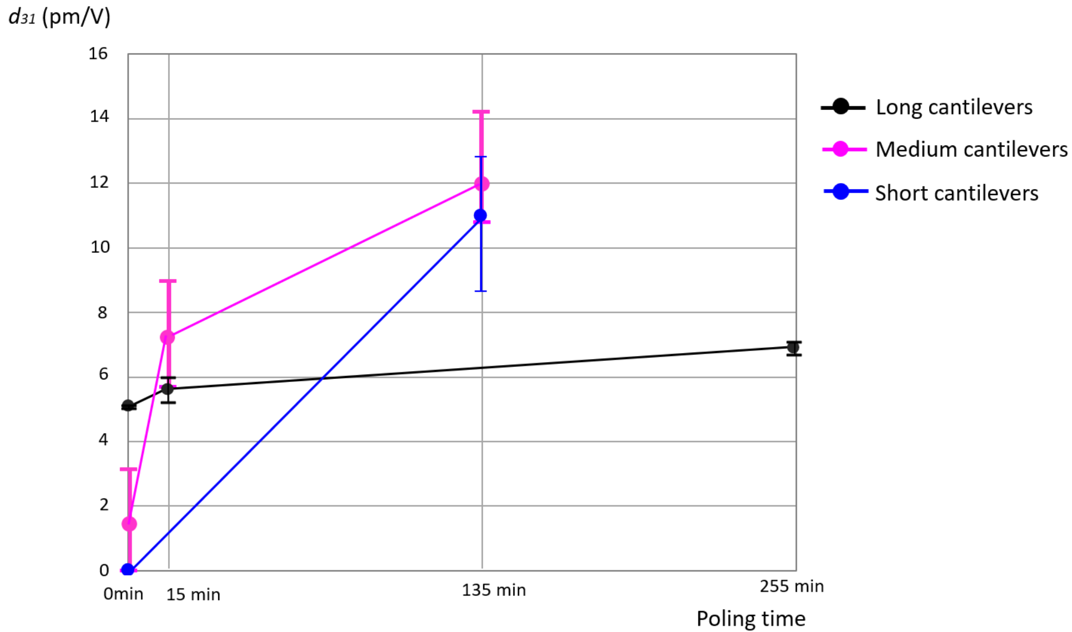

FIG. 12. Evolution of d_{31} (pm/V) as a function of poling time (107 kV/cm at 150°C), for short, medium and long size cantilevers.

TABLE IV. Evolution of d_{31} (pm/V) values, resonance frequencies and Q factor as a function of poling time.

	Poling time	Before poling	15min	135min	255min
Long cantilever 1	d_{31} (pm/V)	5.1	6.0	7.2	7.1
	Resonance (kHz)	18.2	18.0	18.3	18.3
	Q factor (in air)	66	65	67	67
Long cantilever 2	d_{31} (pm/V)	5.00	5.27	NE*	6.7
	Resonance (kHz)	19.5	19.1	NM**	19.1
	Q factor (in air)	67	71	NE	69
Medium cantilever 1	d_{31} (pm/V)	1.2	9.0	14.2	13.9
	Resonance (kHz)	466.6	467.4	473.2	472.9
	Q factor (in air)	208	185	223	228
Medium cantilever 2	d_{31} (pm/V)	3.1	6.9	10.9	NE
	Resonance (kHz)	443.5	442.0	441.4	NM
	Q factor (in air)	109	100	100	NE
Medium cantilever 3	d_{31} (pm/V)	undetectable	5.7	10.8	NE
	Resonance (kHz)		501.0	504.7	NM
	Q factor (in air)		108	103	NE
Short cantilever 1	d_{31} (pm/V)	undetectable	NE	11.5	10.9
	Resonance (MHz)		NM	5.72	5.71
	Q factor (in air)		NE	381	382
Short cantilever 2	d_{31} (pm/V)	undetectable	NE	12.8	NE
	Resonance (MHz)		NM	5.14	NM
	Q factor (in air)		NE	92	NE
Short cantilever 3	d_{31} (pm/V)	undetectable	NE	8.6	NE
	Resonance (MHz)		NM	3.57	NM
	Q factor (in air)		NE	34	NE

*Not Estimated, **Not Measured

Table IV also indicates the changes in resonance frequencies, d_{31} values and quality factors as a function of poling time for long, medium size and short cantilevers. As mentioned in section III. B, poling treatment might lead to either changes in the mechanical characteristics of the PZT films or additional beam curvature. In general, the resonance frequencies of the cantilevers decrease after the first 15 minutes of poling, but after further poling, the resonance frequencies tend to increase along with the d_{31} values.

E. Validation with mechanical frequency response measurements

To validate the d_{31} estimation method, the tip deflection of the cantilevers was measured using a Polytec MSA-500 laser vibrometer. The cantilevers were excited with a voltage signal (a periodic chirp) applied to the PZT and the velocity of several points on the cantilevers were measured. Figure 13 illustrates the deformed shape of a 150 µm long cantilever at its first three resonances, showing excellent qualitative agreement with the theoretical mode shapes of a cantilever beam. Figure 14(a) gives the deformed shape of a 35 µm medium cantilever around its fundamental resonance. To provide more quantitative insight, a detailed view of the anchor with magnified amplitude is also given in Fig. 14(b), showing that, as suspected in section IV. A, the clamping of the cantilever is not perfect. Figures 14(c) and (d) show that the ratio between the maximum amplitude to the amplitude at the theoretical clamping zone (*x=0*) is very small, of the order of 1 %. Similar results for non-ideal clamping have been observed in a reference.[36]

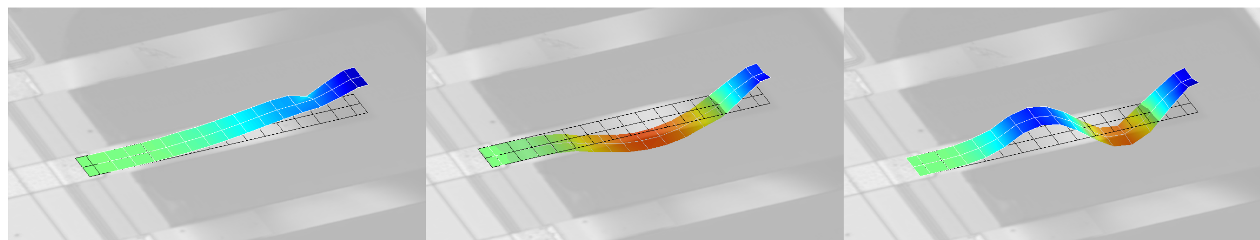

18.34 kHz 102 kHz 292 kHz

FIG. 13. First three bending mode shapes of a 150 µm long cantilever measured with the laser vibrometer.

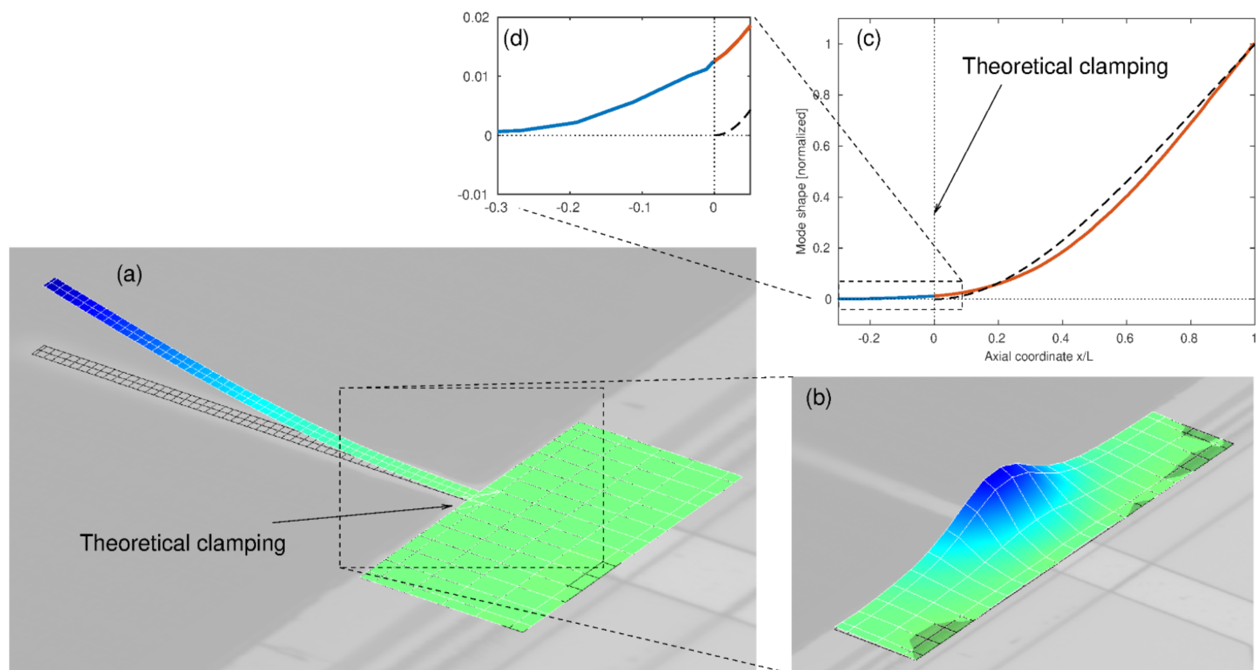

FIG. 14. First bending mode shape of a 35µm long medium cantilever measured with the laser vibrometer at 477.2 kHz. (a) 3D view and (b) zoom on the anchor with magnified amplitude, (c) measured profile (solid line) taken from the 3D view, theoretical deformed shape (dashed line) and (d) zoom in at the anchor area.

The laser was then focused on the tip of a cantilever and the frequency response $H_v(\Omega)$ was determined from the measured velocity signal (obtained by fast Fourier transforms and averaged over time) divided by the input voltage. The results are identical to those obtained with a network analyzer and homodyne detection. Figure 15 shows the tip frequency response of a medium cantilever (with its fundamental resonance around 500 kHz) and of a long cantilever (with its first three resonance peaks). The short cantilevers frequency response was not measured since the maximum detection frequency of the laser vibrometer was 2 MHz, greater than their fundamental frequency.

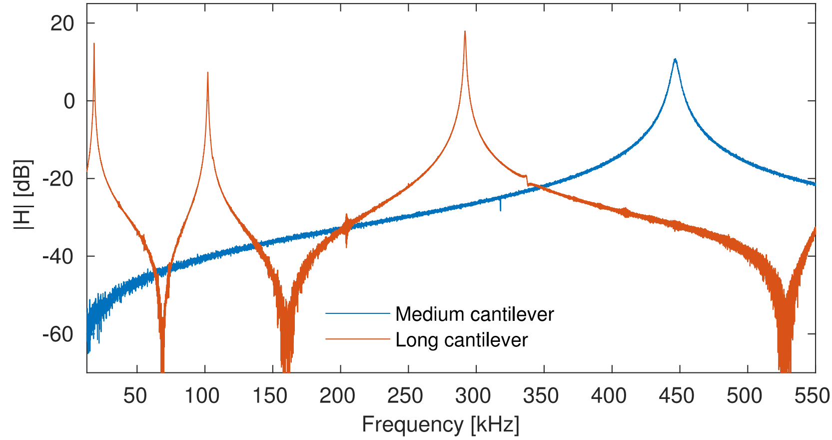

FIG. 15. Experimental frequency response functions: tip displacement of the cantilevers for a unit voltage in the PZT layer as a function of driving frequency, measured by the laser vibrometer.

From the equivalent single layer theory described in the Appendix, the displacement amplitude at the tip of the cantilever w_{t0}, at resonance, is:

$$H(\omega_k) \approx \frac{w_{t0}}{V_0} = \gamma d_{31} \quad \text{with} \quad \gamma = \frac{Q_k Y_p \hat{\hat{\Theta}} \Phi_k(1) \Phi_k'(1)}{mL^2 \omega_k^2}, \tag{4}$$

which allows the piezoelectric constant to be estimated as:

$$d_{31} = \frac{H(\omega_k)}{\gamma}. \tag{5}$$

Around a given resonance, the natural frequency ω_k, the Q-factor and the amplitude of $H_v(\omega_k) = \omega_k H(\omega_k)$ (H_v is the velocity frequency response, whereas H is in displacement) were determined.

Table V shows the estimation of the d_{31} piezoelectric constant obtained from the motional capacitance and the laser vibrometer (mechanical response). The two methods are reasonably close. The measurements of this section were performed about 12 months after those of section IV. D. The obtained values are a little smaller, probably due to aging of the PZT layers.

TABLE V. Estimated values of the d_{31} piezoelectric constant with the motional capacitance method and the mechanical frequency response method for two cantilevers of Table IV.

	Long cantilever 1		Medium cantilever 2
	Mode 1	Mode 3	Mode 1
Natural frequency [kHz]	18.3	291.6	446.8
Quality factor	67	298	223
d_{31} motional capacitance estimation [pm/V]	7.2	8.3	10.9
d_{31} mechanical response estimation [pm/V]	8.7	7.8	6.9

V. CONCLUSIONS

Silicon based cantilevers integrating 281 nm thick microcontact printed $PbZr_{0.3}Ti_{0.7}O_3$ films were fabricated. The resonance frequencies of the cantilevers were detected via the piezoelectric response of the integrated PZT films, thus validating the capability of simultaneous excitation and detection of the PZT cantilevers even at small sizes (e.g. 10 µm-long and 2 µm-wide cantilevers had a resonance frequency of 5.7 MHz and a Q factor of 381 in air). By analytical modelling of the PZT cantilevers and validations of the modelling by finite element simulation, d_{31} was estimated to be around 10 pm/V. Thin PZT films for realization of NEMS have been used for integrated actuation and detection on a geometrically complex elastic structure. This estimation of d_{31} piezoelectric coefficient was consistent with values obtained from the mechanical response measured by a laser vibrometer. Hence, microcontact printed PZT films with poling treatment offer promising transduction schemes for piezoelectric NEMS with integrated actuation and sensing capabilities.

ACKNOWLEDGMENTS

The French General Delegation for Armament and the French National Agency for Research (grant ANR/PNANO 2008, project NEMSPIEZO ‘ANR-08-NANO-015’), and a National Security Science and Engineering Faculty Fellowship are gratefully acknowledged for financial support. Cédric Ayela and Isabelle Dufour from IMS Bordeaux as well as Dolores Manrique from LAAS Toulouse are acknowledged for technical support and open access to the laser vibrometer.

This work was supported by LAAS-CNRS technology platform, a member of Renatech network.

Appendix: single layer equivalent theory

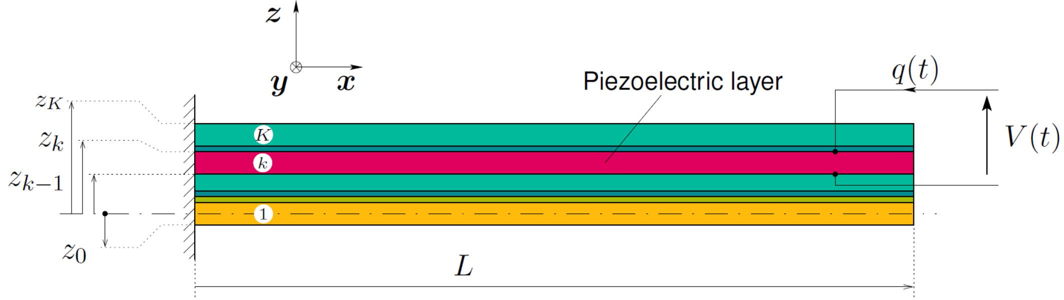

Figure A.1 Sketch of the laminated cantilever beam composed of K layers.

As per the theory,[30] a laminated beam composed of $K \in \mathbb{N}$ elastic layers is considered, where one layer is piezoelectric (Fig. A.1). The beam is clamped at $x = 0$ and free at $x = L$, x being the axial coordinate. The kth layer ($k = 1, \dots K$) is situated between heights z_{k-1} and z_k, z being the bending direction; its thickness is $h_k = z_k - z_{k-1}$ and its width (in the y direction) is b_k. A beam with a uniform cross section over its whole length L is considered. This allows evaluation of an equivalent single layer theory for the beam deformations, with the plane cross section remaining plane and orthogonal to the middle line (Euler-Bernoulli assumptions or classical theory of laminate composites[34]). The deformation of the beam in bending along z is characterized by the transverse displacement field along this direction $w(x,t)$ at time t and axial position x, which is coupled to the voltage difference $V(t)$ between the electrodes of the piezoelectric layer and the electric charge $q(t)$ contained in its upper electrode. With this theory, $w(x,t)$ obeys the following equations:[30]

$$\begin{cases} \widehat{D} w_{,xxxx} + m\ddot{w} + \widehat{\Theta}[\delta(x-L)]_{,x} = 0, & \forall x \in [0 \;\; L] \\ q - \hat{C}V - \widehat{\Theta} w_{,x}\big|_{x=L} = 0, & \end{cases} \tag{A.1}$$

where $\widehat{D}$ is the bending stiffness of the beam, m is its mass per unit length, $\widehat{\Theta}$ is the piezoelectric coupling coefficient, $\hat{C}$ is the blocked electric capacitance of the piezoelectric layer, $\delta(x)$ is the Dirac delta function, $()_{,x} = \partial()/\partial x$ and $\dot{()} = \partial()/\partial t$. The electromechanical characteristics of the beam $m, \widehat{D}, \widehat{\Theta}, \hat{C}$ as a function of the geometrical/material properties of the layers are defined by:

$$\widehat{D} = D - \frac{B^2}{A}, \quad \widehat{\Theta} = \Theta - \frac{B}{A}\Xi, \quad \hat{C} = C + \frac{\Xi^2}{AL}, \tag{A.2}$$

with:

$$m = \sum_{k=1}^{K} b_k h_k \rho_k, \quad A = \sum_{k=1}^{K} b_k h_k Y_k, \quad B = \sum_{k=1}^{K} b_k \frac{z_k^2 - z_{k-1}^2}{2} Y_k, \qquad D = \sum_{k=1}^{K} b_k \frac{z_k^3 - z_{k-1}^3}{2} Y_k, \tag{A.3}$$

$$\Xi = b_p Y_p d_{31}, \qquad \Theta = b_p \frac{z_p + z_{p-1}}{2} Y_p d_{31}, \qquad C = \epsilon_{33} \frac{b_p L}{h_p}, \tag{A.4}$$

where Y_k and ρ_k are the Young's modulus and the mass density of the kth layer, p is the index of the piezoelectric layer and d_{31} and ϵ_{33} are its piezoelectric and dielectric constants. D, A, B are respectively the bending, axial and axial/bending stiffness parameters of the beam; Θ, Ξ are respectively the bending and axial piezoelectric parameters of the beam. The modified parameters that appear in Eqs. (A.1), denoted with a hat $(\widehat{D}, \widehat{\Theta}, \hat{C})$, are independent of the vertical reference $z = 0$ of the lamination, which can be chosen arbitrarily. It is also possible to choose the vertical reference so that $B = 0$, which in this case leads to $\widehat{D} = D$, $\widehat{\Theta} = \Theta$ and $\hat{C} = C$. The reader can refer to a reference[30] for more details.

The eigenmodes of the beam in short circuit ($V = 0$) are defined as follows. The natural frequencies, in [Hz], can be computed from:

$$f_k = \frac{\omega_k}{2\pi}, \text{ with } \omega_k = \frac{\beta_k^2}{L^2} \sqrt{\frac{\widehat{D}}{m}}, \tag{A.5}$$

and the mode shapes are:

$$\Phi_k(\bar{x}) = \cos \beta_k \bar{x} - \cosh \beta_k \bar{x} + \frac{\sin \beta_k - \sinh \beta_k}{\cos \beta_k + \cosh \beta_k} (\sin \beta_k \bar{x} - \sinh \beta_k \bar{x}), \tag{A.6}$$

with $\bar{x} = x/L$. β_k is the kth solution of:

$$\frac{1}{\cosh \beta} + \cos \beta = 0, \tag{A.7}$$

because of the clamped – free boundary conditions, defined by:

$$\Phi_k(0) = 0, \qquad \Phi_k'(0) = 0, \qquad \Phi_k''(1) = 0, \qquad \Phi_k'''(1) = 0, \tag{A.8}$$

where $()' = \mathrm{d}()/\mathrm{d}\,\bar{x}$. With Eq. (A.6), the mode shapes are naturally normalized:

$$\int_0^1 \Phi_k^2(\bar{x}) \, \mathrm{d}\,\bar{x} = 1. \tag{A.9}$$

With the above equations, the frequency parameters, the mode shape amplitude at the tip (the free end) and the slope at the same location are:

$$\begin{gathered} \beta_1 = 1.8751, \qquad \beta_2 = 4.6941, \qquad \beta_3 = 7.8548, \qquad \beta_4 = 10.996 \\ \Phi_k'(1) = 2, \qquad \forall k, \\ \Phi_1'(1) = 2.7530, \qquad \Phi_2'(1) = 9.5616, \qquad \Phi_3'(1) = 15.697, \qquad \Phi_4'(1) = 21.990, \end{gathered} \tag{A.10}$$

The equations of motion (A.1) are now expanded on the kth eigenmode:

$$w(x,t) = \Phi_k(x)\eta(t), \tag{A.11}$$

where $\eta(t)$ is the modal coordinate. Thanks to the orthogonality of the modes, the problem can be written as:

$$\begin{cases} \ddot{\eta} + \dfrac{\omega_k}{Q_k}\dot{\eta} + \omega_k^2\eta - \dfrac{\chi_k}{mL}V = 0 \\ q = \hat{C}V + \underbrace{\chi_k\eta}_{q_{\text{mot}}} \end{cases} \tag{A.12}$$

with the modal piezoelectric coefficient defined by:

$$\chi_k = \frac{\widehat{\Theta}\Phi_k'(1)}{L} \tag{A.13}$$

and where a linear modal damping term has been added, of quality factor Q_k. The motional electric charge q_{mot}, defined in Eq. (A.12), is the part of the electric charge generated by the piezoelectric coupling.

For the frequency response of the cantilever beam, if a sine voltage $V(t) = V_0 \cos \Omega t$ is applied across the piezoelectric layer, the modal coordinate and the motional electric charge are sine functions, that are written $\eta(t) = \text{Re}(\hat{\eta} \exp j\Omega t) = \eta_0 \cos(\Omega t + \varphi)$ and $q_{\text{mot}}(t) = \text{Re}(\hat{q}_{\text{mot}} \exp j\Omega t) = q_0 \cos(\Omega t + \psi)$. With Eq. (A.12), the complex amplitudes $\hat{\eta} = \eta_0 \exp j\varphi$ and $\hat{q}_{\text{mot}} = q_0 \exp j\psi$ can be written:

$$\hat{\eta}(\Omega) = \frac{\chi_k}{mL}\frac{1}{\omega_k^2 - \Omega^2 + 2j\omega_k\Omega/Q_k}V_0, \qquad \hat{q}_{\text{mot}}(\Omega) = \chi_k\hat{\eta}(\Omega). \tag{A.14}$$

Both $\hat{\eta}(\Omega)$ and $\hat{q}_{\text{mot}}(\Omega)$ display a resonant response as a function of Ω.

The response of the cantilever at the resonance frequency, $\Omega \approx \omega_k$, is:

$$\eta_0 = \frac{\chi_k Q_k}{mL\omega_k^2}V_0, \qquad q_0 = \frac{\chi_k^2 Q_k}{mL\omega_k^2}V_0, \tag{A.15}$$

Considering the one-mode approximation of Eq. (A.11) and Eq. (A.13), the amplitude of the tip displacement at the kth resonance can be written:

$$w_{\text{t0}} = \Phi_k(1)\eta_0 = \frac{Q_k\widehat{\Theta}\Phi_k(1)\Phi_k'(1)}{mL^2\omega_k^2}V_0. \tag{A.16}$$

The motional capacitance, defined by the ratio of q_0 and V_0 at resonance,[31] is then:

$$C_{\text{mot}} = \frac{Q_k\widehat{\Theta}^2\Phi_k'^2(1)}{mL^3\omega_k^2} \tag{A.17}$$

Comparing Eqs. (A.2) and (A.4) shows that $\widehat{\Theta}$ is proportional to $Y_p d_{31}$:

$$\widehat{\Theta} = \widehat{\widehat{\Theta}} Y_p d_{31}, \tag{A.18}$$

with $\widehat{\widehat{\Theta}}$ of dimension [m^2]. As a consequence, Eqs. (A.16)-(A.17) can be rewritten:

$$\frac{w_{t0}}{V_0} = \underbrace{\frac{Q_k Y_p \widehat{\widehat{\Theta}} \Phi_k(1) \Phi'_k(1)}{m L^2 \omega_k^2}}_{\gamma} d_{31}, \qquad C_{\mathrm{mot}} = \underbrace{\frac{Q_k Y_p^2 \widehat{\widehat{\Theta}}^2 \Phi'^2_k(1)}{m L^3 \omega_k^2}}_{\alpha} d_{31}^2 \tag{A.19}$$

The parameters γ (dimensionless) and α (homogeneous to [N/m]), depend on the geometrical and material properties of the beam (through parameters Y_p, $\widehat{\widehat{\Theta}}$, m and L) and its kth eigenmode (ω_k, Φ_k, Q_k).

REFERENCES

[1] H. G. Craighead, "Nanoelectromechanical systems," *Science* **290**, 1532-1535 (2000).

[2] M. L. Roukes, "Nanoelectromechanical systems face the future," *Phys. World* **14**, 25-31 (2001).

[3] K. L. Ekinci, "Electromechanical transducers at the nanoscale: actuation and sensing of motion in nanoelectromechanical systems (NEMS)," *Small Journal* **1**, 786–797 (2005).

[4] Y. T. Yang, C. Callegari, X. L. Feng, K. L. Ekinci, and M. L. Roukes, "Zeptogram-scale nanomechanical mass sensing," *Nano Letters* **6**, 583-586 (2006).

[5] J. Chaste, A. Eichler, J. Moser, G. Ceballos, R. Rurali, and A. Bachtold, "A nanomechanical mass sensor with yoctogram resolution," *Nat. Nanotech*. **7**, 301–304 (2012).

[6] J. L. Arlett, E. B. Myers, and M. L. Roukes, "Comparative advantages of mechanical biosensors," *Nature Nanotechnology* **6**. 203-215 (2011).

[7] B. Ilic, Y. Yang, K. Aubin, R. Reichenbach, S. Krylov, and H. G. Craighead, "Enumeration of DNA molecules bound to a nanomechanical oscillator," *Nano Letters* **5**, 925-929 (2005).

[8] Z. J. Davis, G. Abadal, B. Helbo, O. Hansen, F. Campabadal, F. Pérez-Murano, J. Esteve, E. Figueras, J. Verd, N. Barniol, and A. Boisen, "Monolithic integration of mass sensing nano-cantilevers with CMOS circuitry," *Sensors and Actuators A* **105**, 311–319 (2003).

[9] R. B. Karabalin, M. H. Matheny, X. L. Feng, E. Defaÿ, G. Le Rhun, C. Marcoux, S. Hentz, P. Andreucci, and M. L. Roukes, "Piezoelectric nanoelectromechanical resonators based on aluminum nitride thin films," *Appl. Phys. Lett.* **95**, 103111 2009.

[10] N. Sinha, G. E. Wabiszewski, R. Mahameed, V. V. Felmetsger, S. M. Tanner, R. W. Carpick, and G. Piazza, "Piezoelectric aluminum nitride nanoelectromechanical actuators," *Appl. Phys. Lett.* **95**, 053106 (2009).

[11] Z. Qian, F. Liu, Y. Hui, S. Kar, and M. Rinaldi, "Graphene as a massless electrode for ultrahigh-frequency piezoelectric nanoelectromechanical systems," *Nano Lett.* **15**, 4599–4604 (2015).

[12] L. Nicu and T. Leïchlé, "Biosensors and tools for surface functionalization from the macro- to the nanoscale: the way forward," *J. Appl. Phys.* **104**, 111101 (2008).

[13] S. Trolier-McKinstry and P. Muralt, "Thin film piezoelectrics for MEMS," *J. Electroceram.* **12**, 7–17 (2004).

[14] C. Lee, T. Itoh, T. Ohashi, R. Maeda, and T. Suga, "Development of a piezoelectric self-excitation and self-detection mechanism in PZT microcantilevers for dynamic scanning force microscopy in liquid," *Journal of Vacuum Science & Technology B* **15**, 1559-1563 (1997).

[15] T. Itoh, T. Ohashi, and T. Suga, "Piezoelectric cantilever array for multiprobe scanning force microscopy," *IEEE Int. Conference MEMS 1996*, 451-455 (1996).

[16] F. Mathieu, F. Larramendy, D. Dezest, C. Huang, G. Lavallee, S. Miller, C.M. Eichfeld, W. Mansfield, S. Trolier-McKinstry, and L. Nicu, "Reducing parasitic effects of actuation and sensing schemes for piezoelectric microelectromechanical resonators," *Microelec. Eng.* **111**, 68–76 (2013).

[17] S. Guillon, D. Saya, L. Mazenq, J. Costecalde, D. Remiens, C. Soyer, and L. Nicu, "Lead zirconate titanate nanoscale patterning by ultraviolet-based lithography lift-off. technique for nano-electromechanical system applications," *IEEE Trans. Ultrason. Ferroelectr. Freq. Control* **59**, 1955-1961 (2012).

[18] D. Dezest, O. Thomas, F. Mathieu, L. Mazenq, C. Soyer, J. Costecalde, D. Remiens, J.-F. Deü, and L. Nicu, "Wafer-scale fabrication of self-actuated piezoelectric nanoelectromechanical resonators based on lead zirconate titanate (PZT)," *J. Microelec. Microeng.* **25**, 35002-35013 (2015).

[19] A. J. Welsh, R. H.T. Wilke, M. A. Hickner, S. Trolier-McKinstry, "Low-cost, damage-free patterning of lead zirconate titanate films," *J. Am. Ceram. Soc.* **96**, 2799-2805 (2013).

[20] D. Saya, D. Dezest, A.J. Welsh, O. Thomas, F. Mathieu, T. Leichle, L. Nicu and S. Trolier-McKinstry, "Fabrication and characterization of mechanical resonators integrating microcontact printed PZT films", *2017 Joint IEEE–International Symposium on the Applications of Ferroelectric (ISAF)/International Workshop on Acoustic Transduction Materials and Devices (IWATMD)/Piezoresponse Force Microscopy (PFM)*, May 7-11, 2017, Atlanta, USA.

[21] G. Arndt, E. Defay, G. Le Rhun, P. Rey, F. Perruchot, M. Aid, L. Liu, and M. Miller, "Dynamic analytical modelling and piezoelectric characterization of a $Pb(Zr,Ti)O_3$/SiN cantilever with losses," *J. Micromech. Microeng.* **20**, 115019 (2010).

[22] H. G. Yeo, and S. Trolier-McKinstry, "Effect of piezoelectric layer thickness and poling conditions on the performance of cantilever piezoelectric energy harvesters on Ni foils," *Sensors and Actuators A* **273**, 90-97 (2018).

[23] J. F. Shepard Jr, P. J. Moses, and S. Trolier-McKinstry, "The wafer flexure technique for the determination of the transverse piezoelectric coefficient (d_{31}) of PZT thin films," *Sens. & Act. A* **71**, 133-138 (1998).

[24] E. M. A. Fuentes-Fernandez, B. E. Gnade, M. A. Quevedo-Lopez, P. Shah, and H. N. Alshareef "The effect of poling conditions on the performance of piezoelectric energy harvesters fabricated by wet chemistry," *J. Mater. Chem. A* **3**, 9837-9842 (2015).

[25] A. Lebied, B. Necib, and M. Sahli, "Analytical modeling of a piezoelectric bimorph beam", *American Journal of Mechanical Engineering* **4**, 7-10 (2016).

[26] L. H. Kang, D. O. Lee, and J.-H. Han, "A measurement method for piezoelectric material properties under longitudinal compressive stress–a compression test method for thin piezoelectric materials," *Measurement Science and Technology* **22**, 065701 (2011).

[27] C. M. Costa, V. Sencadas, J. F. Mano, and S. Lanceros-Méndez, "Effect of poling on the mechanical properties of β-poly(vinylidene fluoride)," *Materials Science Forum* **514-516**, 951-955 (2006).

[28] J. F. Shepard. F. Chu, I. Kanno, and S. Trolier-McKinstry, "Characterization and aging response of the d31 piezoelectric coefficient of lead zirconate titanate thin films," *Journal of Applied Physics* **85**, 6711-6716 (1999).

[29] A. Kholkin, E. Colla, K. Brooks, P. Muralt, M. Kohli, T. Maeder, D. Taylor, and N. Setter, "Interferometric study of piezoelectric degradation in ferroelectric thin films," *Microelectronic Engineering* **29**, 261-264 (1995).

[30] J. Ducarne, O. Thomas, and J. F. Deü, "Placement and dimension optimization of shunted piezoelectric patches for vibration reduction," *J. Sound Vib.* **331**, 3286–3303 (2012).

[31] O. Thomas, B. Legrand, and C. Fuinel, "Optimization of length and thickness of smart transduction layers on beam structures for control and M/NEMS applications," *SMASIS 2015 Colorado Springs*, USA, Sept. 2015, 8857.

[32] D. Das, L. Sanchez, J. Martin, B. Power, S. Isaacson, R. G. Polcawich, and I. Chasiotis, "Control of mechanical response of freestanding $PbZr_{0.52}Ti_{0.48}O_3$ films through texture," *Appl. Phys. Lett.* **109**, 131905 (2016).

[33] http://www.makeitfrom.com/material-properties/Hafnia-Hafnium-Oxide-HfO2

[34] O. Thomas, J.-F. Deü, and J. Ducarne, "Vibration of an elastic structure with shunted piezoelectric patches: efficient finite-element formulation and electromechanical coupling coefficients," *International Journal of Numerical Methods in Engineering* **80**, 235–268 (2009).

[35] H. Miki, K. Kushida-Abdelghafar, K. Torii, and Y. Fujisaki, "Hydrogen-related degradation and recovery phenomena in $Pb(Zr,Ti)O_3$ capacitors with a platinum electrode," *Japanese Journal of Applied Physics* **36**,1132-1135 (1997).

[36] J.N. Reddy, "Mechanics of laminated composite plates and shells: theory and analysis," *CRC Press,* (1997).